Hindawi
Advances in Civil Engineering
Volume 2019, Article ID 3561395, 12 pages
https://doi.org/10.1155/2019/3561395

Research Article

Experimental Investigation on Fracture Evolution in Sandstone Containing an Intersecting Hole under Compression Using DIC Technique

Hao Wu,[1,2] **Guoyan Zhao**,[1] **Weizhang Liang**,[1] **Enjie Wang**,[1] **and Shaowei Ma**[1]

[1]*School of Resources and Safety Engineering, Central South University, Changsha, Hunan 410083, China*
[2]*Department of Mining and Geological Engineering, The University of Arizona, Tucson, AZ 85721, USA*

Correspondence should be addressed to Guoyan Zhao; gy.zhao@csu.edu.cn

Received 22 December 2018; Accepted 12 March 2019; Published 7 April 2019

Academic Editor: Hugo Rodrigues

Failure of underground structures, especially intersections, becomes more severe as the depth increases, which poses a new challenge for the safe construction and operation of deep rock engineering. To investigate the mechanical properties and fracture behavior of rock with an intersecting hole under compressive loads, a series of uniaxial compression tests was carried out on cuboid red sandstone specimens containing an intersecting hole with three types of shapes by digital image correlation (DIC) technique. The results showed that the existing hole inside specimens leads to almost a 50% reduction of mechanical parameters from that of intact ones, and this weakening effect is associated with the shapes of holes. Failure of specimens is a progressive process in which cracks, i.e., primary tensile cracks, secondary tensile cracks, and shear cracks, initiate from stress concentration zones, propagate along certain direction, and coalesce with each other into macrofractures. Both the real-time principal strain fields and horizontal displacement fields of specimens under compression could be visually displayed by DIC system, and they were in good consistency in characterizing the fracture behavior. Moreover, the propagation characteristics of primary tensile cracks were studied further by quantitatively analyzing the strain variation during the loading process, and the propagation mechanism of "open-close-reopen" of primary tensile cracks was explained in detail.

1. Introduction

Underground mining is a process of bringing earth minerals to the surface. It is commonly understood that digging a large number of roadways or shafts into the earth to reach ore deposits is essential [1–4]. Just like road intersections in traffic engineering, there are also junctions between shafts and roadways in underground mines. For example, the intersection formed by two roadways, the inset connecting a vertical shaft and a pit bottom, as well as the junction between a roadway and a winze used for ore drawing, ventilation, filling, pedestrian passageway, etc [5–7]. However, failure of roofs and ribs occurs frequently at intersections due to the large exposed area of surrounding rock, high degree of stress concentration, and strong disturbance caused by multiple times of excavation. As a result, intersection structures usually need repair or secondary reinforced support to ensure their stability, which seriously affect the production schedule. Therefore, studying the stability and failure mechanism of intersection structures is particularly necessary, playing a significant role in support design of mines.

According to the literature, scholars have carried out extensive researches on the stability and support technology of roadway intersections. During the late 1980s, the United States Mines Bureau did a survey and found that more than 30% of roof falls occurred at roadway intersections. The surrounding rock of four-way intersections had the worst stability, and the maximum settlement of roofs was about twice that of three-way intersections [8]. Okubo and Peng [9] found that an arching zone was formed above three-way intersections, and a region of vertical tensile stress was developed over a short distance into the roof. Gerçek [5, 10] deemed that the higher the

horizontal stress and the more complex the intersection structures, the worse the roof stability at intersections. Hematain [11] proposed two formulas for calculating the bottom radius and the height of dome-shaped roof over four-way intersections. Singh et al. [12] analyzed the mechanical behavior of three-way intersections under a range of loading conditions. As a driving force of deformation, geostress has a pronounced influence on the stability of intersection structures. Researches showed that failure modes of roadway intersections are highly dependent on the horizontal stress [13, 14]. Besides, many numerical software applications, e.g., Flac3d, Ansys, and Abaqus, were applied to assess factors affecting the stability of roadway intersections. The results indicated that the in situ stress or depth, rock strength, width and height of opening, sequence and advance of excavation, and type and angle of intersections had different degrees of effect on the structures' behavior [15–19]. For the secondary support design of intersection structures after deformation, Huang and Kong [20] designed a roof reinforcement scheme by chemical grouting and anchor cables. According to the work of Wang et al. [21], a comprehensive support technology was developed by combining grouting, 3D anchor cables, and prestressed truss. Wang et al. [22] also proposed a double-control bolt support technique in light of the idea of strong support, which achieved a good support effect.

In addition to roadway intersections, intersections between shafts and roadways are also very common in mines. He et al. [23] studied the stress and displacement characteristics of the surrounding rock of pump chambers and found that the excavation sequence of "branch roadway first, main roadway second" had the least disturbance effect on the intersection structure. Guo et al. [24] believed that the instability of deep chambers was the combined result of high geostress, irrational layout, and unmatched support methods. To reveal the evolution process of stress and displacement in surrounding rock of a shaft inset, a group of physical simulation experiments was performed by Li [25]. Results demonstrated that, during the process of unloading induced by excavation, the stress and displacement in rock mass above the junction structure nonlinearly reduced and increased, respectively. Cheng et al. [26] further investigated the distribution of the mining-induced stress field and plastic zone of the intersection structure by numerical simulations and presented a joint support technology, i.e., anchor-net-shotcrete for preliminary bracing and grouting for secondary support. From the above, it is concluded that previous researches mainly focus on repair technologies of intersection structures after failure or large deformation. However, limited studies can be found regarding the fracture evolution and failure mechanism of intersection structures in underground mine. In essence, the instability of rock structures can be regarded as a process of cracks initiation, propagation, and coalescence with each other into macrofailure under different stress conditions. Besides, the mechanical properties of deep rock are completely different from that of shallow rock because of the complicated environmental characteristics, e.g., high stress, high temperature, high seepage pressure, and strong mining disturbance [27–29]. Thus, it addresses a need to systematically study the fracture responses of intersection structures to provide a reference for support design for deep mining.

In the present work, we conducted a series of uniaxial compression tests on rock specimens containing an intersecting hole to investigate the effects of intersection types and the mechanical properties of specimens with open-hole defects were compared with intact specimens. The failure mechanism and crack behavior under the action of uniaxial compression stress were further analyzed in detail by means of digital image correlation (DIC) technique.

2. Experiment Program

2.1. Intersection Structure Simplification. The stability of roadway intersections with the same cross-sectional area and different intersection angles has been widely studied while that of different cross-sectional area has not been fully understood, and further investigations on their fracture characteristics are needed. Therefore, three representative types of intersection structures with an angle of 90° were chosen for research, namely, three-way intersections (TI), four-way intersections (FI), and shaft-roadway intersections (SI), as shown in Figure 1.

In general, main roadways and branch roadways in mines usually have a horseshoe shape with a width to sidewall height ratio of 4 : 1. Since the three-dimensional cracks of rock are difficult to be observed using current testing techniques, the plane stress assumption can be applied to simplify this problem. Based on the symmetry planes of intersection structures, the cuboid red sandstone specimens containing an intersecting hole, whose cross-sectional areas are equal, were prepared for compression tests. The detailed dimensions are shown in Figure 1.

2.2. Specimen Preparation. A total of 12 specimens cut from a fine-grained sandstone block were prepared in four groups, which were named IS, TI, FI, and SI, respectively. Each group contained three specimens. Group IS were intact specimens regarded as the reference. The other three groups were specimens with a hole, corresponding to the ones shown in Figure 1. The dimensions of specimens were determined as $100 \times 25 \times 150$ mm (length × width × height) and the central intersecting hole in specimens were excavated by a waterjet cutting machine. To minimize the experimental errors, ends and surfaces of these specimens were polished smooth with surface flatness less than 0.02 mm and deviation of the verticality between adjacent surfaces less than 0.001 radians, which were in accordance with the standards suggested by the International Society for Rock Mechanics (ISRM) [30]. The detailed parameters of specimens are listed in Table 1.

In addition, according to the ISRM suggested methods for rock testing [30], many kinds of specimens were prepared to measure the basic mechanical parameters of this rock, including 3 cylindrical specimens with a diameter of 50 mm and a height of 100 mm for uniaxial compression

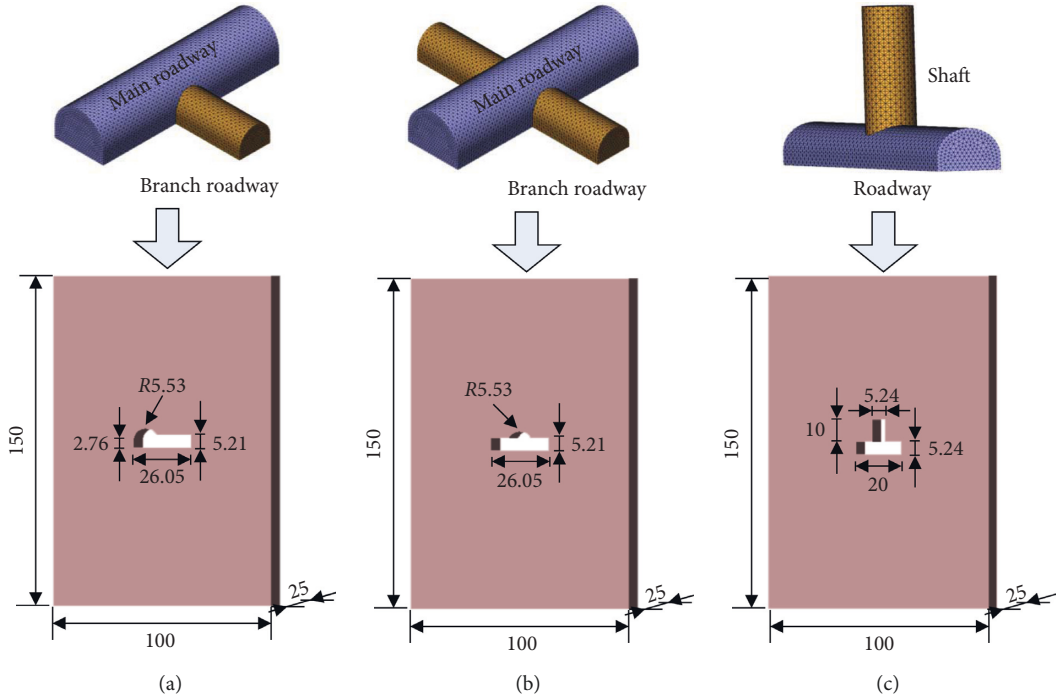

Figure 1: Simplified schematic of the three-dimensional intersection structures by the plane stress assumption: (a) TI; (b) FI; (c) SI.

Table 1: Basic parameters of specimens.

Specimen no.	Density (kg·m^{-3})	Length (mm)	Width (mm)	Height (mm)	Hole area (mm^2)	Note
IS-1	2391.37	100.10	25.00	150.10	0.00	Intact specimens
IS-2	2427.49	99.60	24.90	150.50		
IS-3	2467.45	100.70	24.80	150.70		
TI-1	2382.43	100.50	23.00	150.80	156.58	Specimens containing a three-way intersecting hole
TI-2	2408.37	100.20	24.80	151.00		
TI-3	2439.81	100.40	24.70	150.90		
FI-1	2461.65	100.30	25.00	151.00	157.08	Specimens containing a four-way intersecting hole
FI-2	2439.30	100.40	23.50	150.60		
FI-3	2430.60	100.50	25.00	150.50		
SI-1	2424.91	100.20	25.00	150.70	157.20	Specimens containing a shaft-roadway intersecting hole
SI-2	2433.99	100.30	25.80	150.80		
SI-3	2411.55	100.60	23.40	150.50		

tests, 3 disk specimens with dimensions of 25 × 50 mm (thickness × diameter) for Brazilian tests, and 15 cuboid specimens with dimensions of 50 × 50 × 50 mm for variable-angle shear tests. All tests were performed in displacement-control mode at a constant loading speed of 0.6 mm/min. The uniaxial compressive strength (UCS), Young's modulus, and Poisson's ratio could be calculated based on stress-strain curves obtained from the uniaxial compression tests, which are 99.32 MPa, 24.35 GPa, and 0.26, respectively. The tensile strength is determined as 5.28 MPa by the Brazilian tests. On the basis of the results of the shear tests, the Mohr–Coulomb criterion was applied to calculate the cohesion and friction angle, whose values are 19.01 MPa and 40.43°, respectively. Moreover, the P-wave velocities of specimens were also measured by a SYC-2 acoustic wave rock parameter test instrument, and the average value is 3174.51 m/s.

2.3. Experimental Apparatus. Uniaxial compression tests on sandstone specimens were carried out by an Instron 1346 rock mechanics servocontrolled testing system, and a DIC system and one light source were also used to monitor the fracture evolution during the loading process. The schematic diagram of experimental apparatus is illustrated in Figure 2.

Instron 1346 is widely used in materials and mechanics for compression, tensile, shear, and bending tests. The maximum applied load and relative error are 2000 kN and 0.5%, respectively. All uniaxial compression experiments were conducted at a loading rate of 0.6 mm/min under displacement-controlled conditions. During the tests, the axial loads were automatically monitored and recorded in real time by the testing machine, and the axial displacements of specimens were simultaneously measured by an extra-linear variable differential transformer.

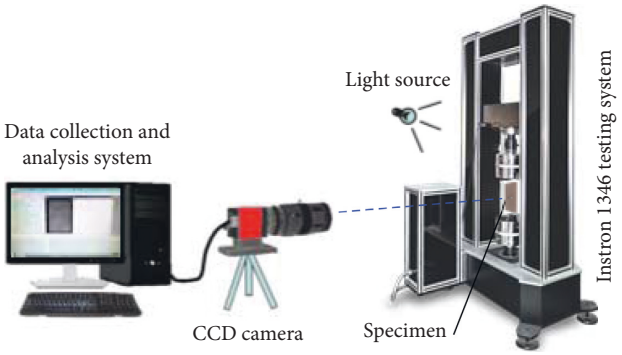

Figure 2: Schematic diagram of experimental apparatus.

DIC, as an optical and noncontact measurement technique, was developed in the 1980s [31, 32]. Due to the advantages such as the simple equipment, strong anti-interference ability, wide measuring range, and efficient identification of strain localization, DIC has become a promising method to obtain the full-field displacement and strain of various solid materials. Accordingly, the fracture evolution of rock specimens during loading could be derived by the DIC system. Before the experiments, artificial speckles are needed to be fabricated on the precleaned observed surfaces of specimens. Hence, the white paint was first used to spray on the surface to form a thin uniform background. After drying, the white paint layer was randomly atomized with black paint by a professional worker. Afterwards, the randomly distributed speckles with good quality on the surfaces were formed. Based on the principle that the grayscale value of pixel stays constant during the test [33, 34], the movements of speckles can be tracked through the comparison of the deformed images and the reference image. The calculation procedure of displacement and strain can be operated by GOM correlate software, including the following steps (Figure 3): (1) choose the speckle image before deformation as a reference and a deformed image as the target, and then select the same observation region in two images; (2) divide the region into many subsets with certain sizes, and determine the initial locations of the subsets; (3) based on the above principle, search for the matched target subsets in the deformed image by correlation algorithms, and calculate the displacements of all subsets; and (4) generate the strain or displacement fields through postprocessing.

In the study, a charged couple device (CCD) camera (Basler/piA2400-17 gm) with a resolution of 2456×2058 pixels was placed perpendicularly to the speckle surface of specimens at a distance of about 1 m. To capture clear images during tests, the camera aperture needed to be adjusted to the best state, and a white table lamp was located on the loading platform to provide a bright light. By the control of Pylon Viewer software installed on the computer, the dimensions of captured images were set as 1100×1500 pixels (width $\times$ height), and the images were continuously recorded at a rate of 15 frames/s. To meet the requirements of data synchronization, the DIC system and the rock mechanics testing system should be started simultaneously.

3. Experimental Results and Discussion

3.1. Mechanical Properties of Specimens under Uniaxial Compression. Based on the recorded data, the stress-strain curve of one typical specimen in each group is plotted in Figure 4. It can be seen that hole defects have a remarkable weakening effect on rock strength. Table 2 presents the results of mechanical parameters of all specimens. The average UCS values of groups IS, TI, FI, and SI are 102.61 MPa, 61.64 MPa, 64.31 MPa, and 46.01 MPa, respectively. Compared with the intact specimens, the UCS of specimens with an intersecting hole could reduce up to 45%–63%. Evidently, the shapes of holes are responsible for the reduction, and the less rounded the hole boundaries, the lower the strength of specimens. A possible reason to explain this phenomenon is that stress concentration is easy to occur at corners. Figure 4 further shows that, for specimens containing a hole, there is a stress oscillation before the peak on the stress-strain curve, which is caused by sudden appearance of cracks. At the postpeak stage, stresses decrease linearly and steeply, and the residual strength of all specimens is approximately zero, suggesting that the specimens are extremely brittle and the elastic energy accumulated in the rock before the peak will suddenly release in this stage. Consequently, the hard rock needs to be supported or reinforced immediately after excavation in deep rock engineering.

Based on the stress-strain curves, the deformation process can be divided into four stages: initial pores compaction and cracks initiation stage (OA), linear deformation stage (AB), unstable fracture stage (BC), and postpeak stage (CD). It is found that periods of the last two stages are very short, showing that the rock is hard and its deformation is small. Figure 5 demonstrates the calculation results of Young's modulus and peak strain. It is concluded that the variation of Young's modulus and peak strain follow the same trend of UCS, which can be ranked as follows: specimens IS > specimens FI > specimens SI > specimens TI.

Previous researches showed that the energy in rock is always changing during deformation, and the essence of brittle failure is the instability driven by sudden change of energy dissipation under the high stress condition [35]. It is commonly recognized that rock specimens will absorb energy at the prepeak stage and then release it at the postpeak stage. Hence, studying the mechanical behavior of rocks from an energy perspective can well explain the rock failure characteristics. We hereby define an energy coefficient of brittleness k to characterize the degree of rock brittleness, which can be expressed by

$$k = \frac{e_a}{e_b} = \frac{\int_{\varepsilon_p}^{\varepsilon_{max}} \sigma \, d\varepsilon}{\int_0^{\varepsilon_p} \sigma \, d\varepsilon}, \quad (1)$$

where e_b and e_a denote the absorbed energy density at the prepeak stage and the released energy density at the postpeak stage of specimens, respectively; σ is the axial stress; ε, ε_p, and ε_{max} represent the axial strain, peak strain, and maximum strain, respectively.

It is generally accepted that the value of k represents the release speed of restored elastic energy in the specimen at the

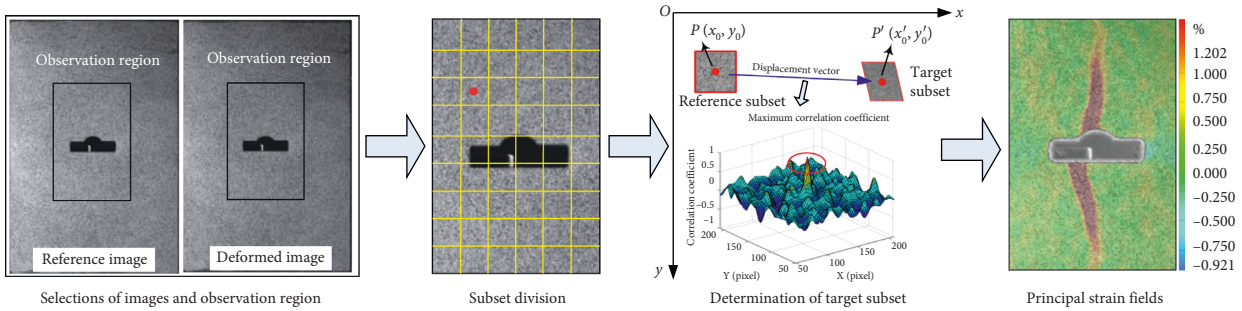

Figure 3: Procedures of DIC calculation.

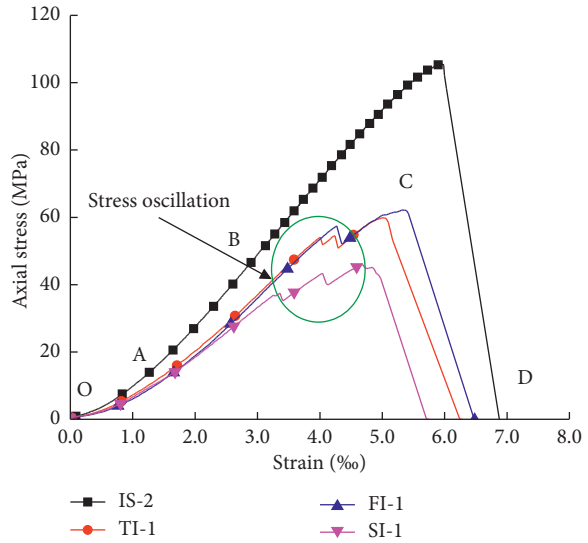

Figure 4: Axial stress-strain curves of four typical specimens under uniaxial compression.

Table 2: Experimental results of specimens under axial compression.

Specimen no.	UCS (MPa)	ε_p (‰)	E (GPa)	e_b (kJ·m^{-3})	e_a (kJ·m^{-3})	k	Failure characteristics
IS-1	100.92	5.57	21.63	100.28	55.38	0.21	Block ejections were observed on the left and right sides of specimens
IS-2	105.61	5.96	21.63	111.42	47.78	0.16	
IS-3	101.31	6.97	20.05	114.90	−88.33	/	Unloading and rebound happened at the postpeak stage
TI-1	59.82	5.01	17.82	50.92	36.24	0.25	Spalling fracture appeared first on two sidewalls of the hole, and then macrofailure occurred along with a loud noise and violent rock ejections due to crack coalescence at the postpeak stage
TI-2	58.47	5.10	17.48	58.33	8.56	0.06	
TI-3	66.64	4.03	18.48	61.45	77.97	0.48	
FI-1	62.10	5.34	18.49	61.65	35.95	0.22	
FI-2	65.30	4.77	19.01	56.08	39.12	0.25	
FI-3	65.54	5.35	18.09	63.71	29.84	0.18	
SI-1	45.92	4.69	14.91	39.43	29.29	0.27	
SI-2	45.85	3.29	15.64	37.97	14.38	0.14	
SI-3	46.25	5.22	14.46	39.65	19.73	0.17	

postpeak stage. The smaller the k value, the faster the elastic energy released, that is, the more brittle the specimen. The calculated results of energy parameters are listed in Table 2. As can be observed, all specimens have small values, and the values of specimens containing an intersecting hole are bigger than the intact samples. The average k values of the four types of specimens are 0.18, 0.26, 0.21, and 0.20, respectively. Thus, the order of brittleness of the four types of specimens can be obtained, i.e., specimens IS > specimens SI > specimens FI > specimens TI. It is noted that specimen IS-3 is unloaded and rebounded at the postpeak stage, so its k value is not valid. From the above, we can conclude that the existence of holes leads to an increase in brittleness of the rock. This is because the corners and tips of hole defects are easily concentrated by stress under compression, accelerating the initiation, propagation, and coalescence of cracks.

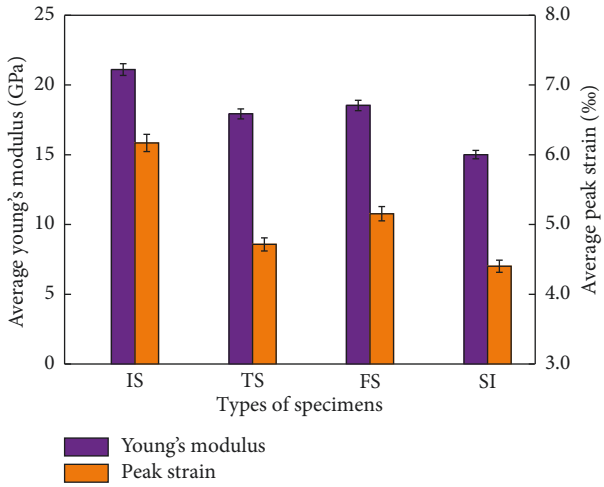

Figure 5: Deformation parameters of different specimens under uniaxial compression.

Therefore, the brittleness of rock specimens with a hole is more significant than the intact ones.

3.2. Reliability Verification of DIC Technique. Researches showed that fracture behavior of rock specimens can be well reflected by strain localization zone [36]. The place where the principal strain is large is likely to initiate cracks. To verify the reliability of DIC system, three groups of 6 strain gauges were strategically attached to the back surface of each intact specimen, three of which were used to measure the horizontal strains and the other three were for the vertical strains. These strain gauges were connected to six channels of DH3818S static strain meter by wires. The instrument should be started simultaneously with the testing apparatus. Figure 6 presents the detailed locations of six monitoring points (A′, B′, C′, D′, E′, and F′) on the front surface and six corresponding monitoring points (A, B, C, D, E, and F) on the back surface of specimen IS-2. The horizontal and vertical real-time strains of points on the front surface of specimens can be fetched by GOM correlate software. As shown in Figure 7, the strain increases gradually over time and suddenly increases to infinity when the experiment ends. The values of strain measured by two methods are very close. This proves that DIC technique is reliable and effective. However, we also observe that the strain of point E′ by DIC technique is larger than that of point E by the strain gauge at the end of experiment, which is caused by surface spalling of part area on the front surface of the specimen in the process of crack propagation.

3.3. Fracture Evolution and Deformation Analysis of Specimens under Axial Loads. It is well known that a variety of defects are commonly distributed in rock mass, such as joints or cracks, weak planes, and voids. Tips and corners of those flaws are easily concentrated by stress under the action of loads, resulting in the formation, propagation, and coalescence of cracks. From the laboratory tests, the strength and deformation characteristics of specimens are related to

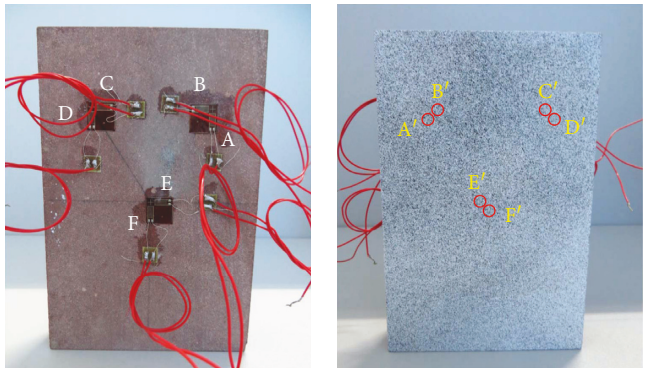

Figure 6: Locations of strain monitoring points on specimen IS-2: (a) back surface; (b) front speckle surface.

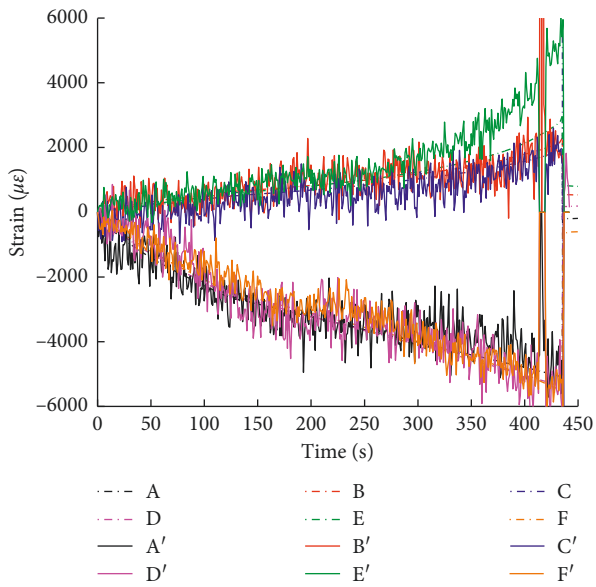

Figure 7: Comparison of strain values measured by strain gauges and DIC technique.

these flaws. Essentially, the damage and failure of rock can be considered as a process in which cracks initiate from these defects, and propagate, nucleate, and coalesce with each other into macrofractures. Therefore, investigations on fracture responses are greatly meaningful to analyze failure mechanism of rock subjected to loads and control hazards of rock engineering.

Based on the images recorded by DIC system, the fracture characteristics and failure modes of one typical specimen in each group were investigated. The evolution of principal strain field of four representative specimens during the loading process are illustrated in Figure 8. For each specimen, five images of principal strain contours at different stress stages corresponding to four deformation stages and peak moment in Figure 4 were selected for analysis and contrast. The numbers shown in subfigures denote the patterns of cracks, while the superscript lowercase letters mean the emergence sequences of the same type of cracks. In

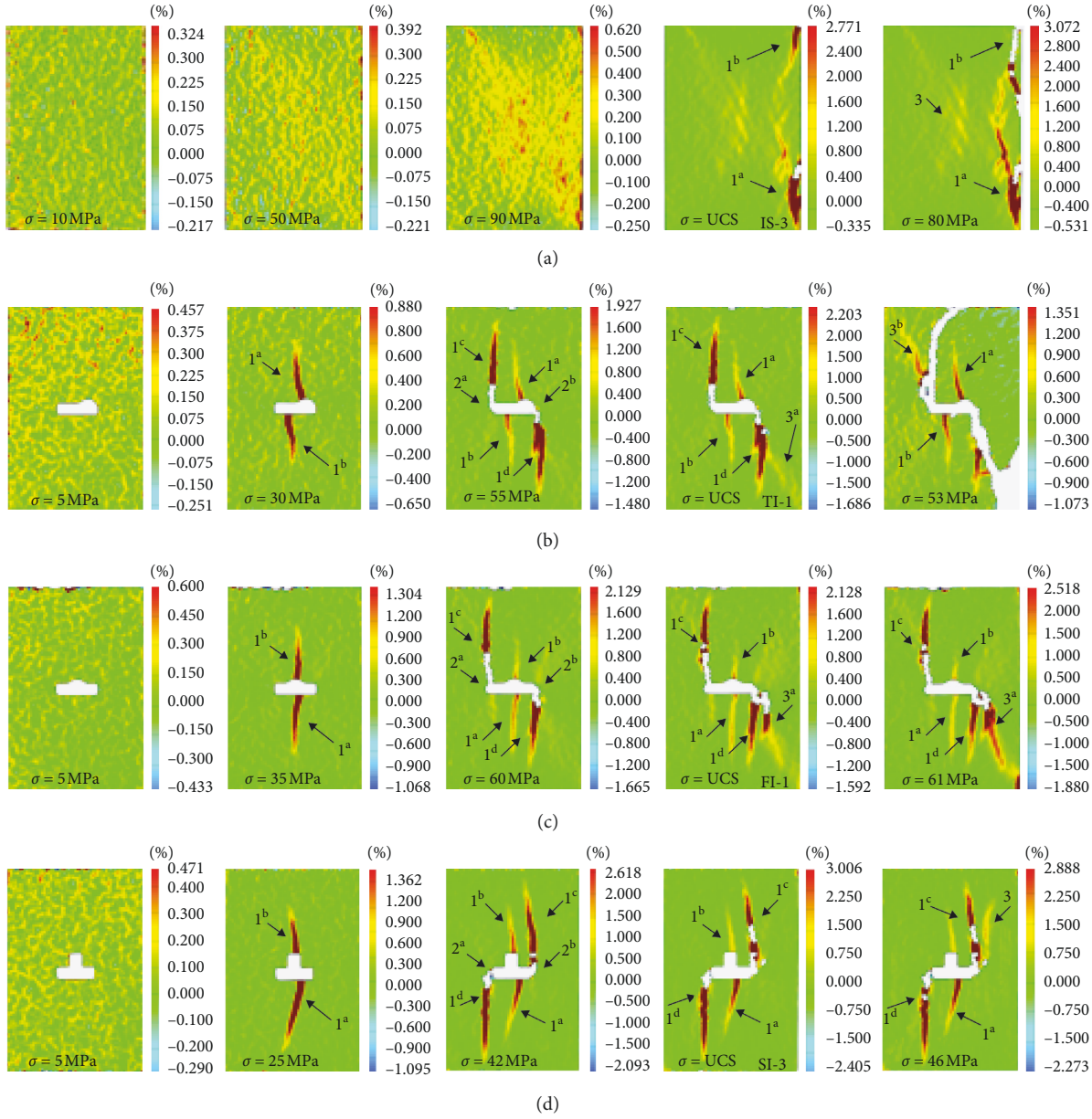

Figure 8: Fracture evolution of different specimens under axial loads: (a) specimen IS-3; (b) specimen TI-1; (c) specimen FI-1; (d) specimen SI-3.

the legend, the positive strain represents the region or point is subjected to a tensile stress, while the negative strain is caused by a compressive stress.

3.3.1. Specimen IS-3. As presented in Figure 8(a), some randomly distributed points with relatively small strain are first formed at the initial pores compaction stage. When the axial stress reaches 50 MPa, the average value of the principal strain is 0.101%. According to the maximum principal strain criterion, the critical tensile strain (ε_t) can be calculated as $\varepsilon_t = \sigma_t/E = 2.17 \times 10^{-4}$, which is far exceeded by the principal strain. However, no macrocracks emerge in this case. It is believed that the density and range of microfractures are not big enough. With the increase of axial stress to 90 MPa, the apparent strain concentrations on the diagonal and right parts of the specimen are observed, and the new formed microcracks could be identified visually. This moment the average principal strain is 0.205%. When the stress reaches the peak, the specimen remains intact, with only two tensile cracks (splitting cracks 1^a and 1^b) initiating in the upper-right and lower-right corners, respectively, and propagating along the loading direction. At the postpeak stage, an oblique crack 3 considered as a shear crack appears and coalesces with cracks 1^a and 1^b, leading to the sudden failure of the specimen, along with a loud noise and violent rock ejections.

3.3.2. Specimen TI-1. According to Figure 8(b), at first, there are many sporadic yellow dots, indicating the pores embedded in the specimen are gradually closed under

compression. It could also be seen that there are many high-strain points concentrated in the top locations of the specimens due to end effects. When the stress approaches 30 MPa, tensile cracks 1^a and 1^b initiate from the top and bottom positions of the specimen and propagate in parallel with the loading direction. With continuous increase of stress, severe spalling zones 2^a and 2^b are formed on both sidewalls of the hole, indicating that the sidewalls suffer from a high level of compressive stress. Afterwards, two secondary tensile cracks 1^c and 1^d parallel to the loading direction appear abruptly under the tensile stress concentration, and they extend from the upper-left and lower-right corners of the hole to the upper and lower boundaries of the specimen, respectively. As a result, there is a corresponding stress fluctuation on the stress-strain curve. Meanwhile, the two primary tensile cracks close gradually. Besides, the blank area around holes is caused by surface spalling in the rapid propagation of secondary cracks. At the peak stress, a far-field crack 3^a initiates from the lower-right part of the specimen and tends to propagate towards the diagonal of the specimen. The secondary cracks continue to develop under compressive loads, and the primary tensile cracks almost disappear. At the postpeak stage, macroscopic failure takes place when the shear cracks 3^a or 3^b intersect with the secondary cracks. Some speckles on the lower-right corner of the specimen are missing due to surface spalling. After failure, it is clearly observed that the two primary tensile cracks reopen again.

3.3.3. Specimen FI-1. As shown in Figure 8(c), specimen FI-1 experiences the same process of fracture evolution with specimen TI-1; that is, fracture proceeds from primary tensile cracks through spalling fracture and secondary tensile cracks to shear fracture under uniaxial compression. However, the originated locations of two primary tensile cracks are different from that of specimen TI-1, which is resulted from the different stress distribution around the holes of specimens.

3.3.4. Specimen SI-3. Compared with the above specimens with a hole, specimen SI-3 has the similar fracture behavior under uniaxial compression, which is shown in Figure 8(d). For specimen SI-3, the average strain values at all stages are the maximum among the four types of specimens. The variation law of principal strain for each specimen during loading is in good agreement; i.e., the average value first increases as stress increases before the peak and then decrease slowly at the postpeak stage.

In addition, we also obtained the horizontal displacement fields by GOM correlate software based on the recorded speckle images. Figure 9 shows the displacement evolution process of four typical specimens at different stress levels corresponding to that in Figure 8. In view of intact specimens, a blue zone emerges first in the left part of the specimen, indicating that this part of rock moves towards the left boundary, and the displacement gradually increases with the increase of axial stress. When the stress reaches 90 MPa, a V-shaped zone symmetrical to the left blue zone appears in the right part of the specimen. The displacement of two areas keep rising until macro splitting-shear failure takes place. For specimens with a hole, at the beginning of loading, the deformation is small. After that, two borderlines are formed on the roof and floor of the cavity, dividing the specimen into two different color parts. The horizontal displacement in the left part is negative, while that in the right part is positive. This indicates that the primary tensile cracks appear due to tensile stress concentration. Similarly, with increasing loads, the other two vertical borderlines representing the secondary tensile cracks emerge from the upper and lower corners of the hole. Meanwhile, the above two borderlines at the top and bottom locations of cavities gradually fade away. As stress increases further, a distinct diagonal line appears gradually, suggesting the formation of shear cracks. The displacement gradient in the vicinity of the line is very clear at the postpeak stage. Finally, macroshear failure occurs along this line. In summary, the real-time deformation of rock specimens under compressive loads can also be well displayed by DIC technique, and the displacement development of rock specimens agrees well with the evolution of fracture.

3.4. Failure Modes of Specimens under Uniaxial Loading. In general, the cracks represented by strain concentration regime are clearly displayed by DIC technique, which provides a new research method for rock fracture mechanics. Figure 8 further manifests that macrofailure of all specimens appears at the postpeak stage rather than at the peak stress. Figure 10 shows the ultimate failure patterns of four types of specimens. The black lines represent the microcracks which are not easy to be identified on the speckle images, while the red lines indicate the main failure paths.

For intact specimens, two splitting cracks first originate from the upper-right and lower-right corners, respectively, and propagate towards each other along the loading direction. When they are connected together, some small blocks of rock eject outward from the right side of specimens. Subsequently, shear crack appears on the diagonal of specimens and coalesces with the linked two splitting cracks, resulting in the final tensile-shear failure. With respect to specimens containing a hole, their crack patterns under progressive axial loads are almost the same. At first, two tensile cracks are first observed on the roof and floor of the cavity, but they are not responsible for the final failure of the specimens. In fact, the failure is resulted from the coalescence of the secondary tensile cracks with the shear ones, and the mode can be considered as shear failure. As can be seen from Figure 10 further, severe surface spalling induced by high concentrated compressive stress occurs near the center of the intact specimen at the postpeak stage. Besides, a crack propagating to the upper boundary is also observed, but it does not run through the full thickness of the specimen, which has little effect on the final failure. In addition, partial secondary cracks of specimens with a hole are found to extend to the upper or lower boundary. This is caused by sharply unloading at the time of failure.

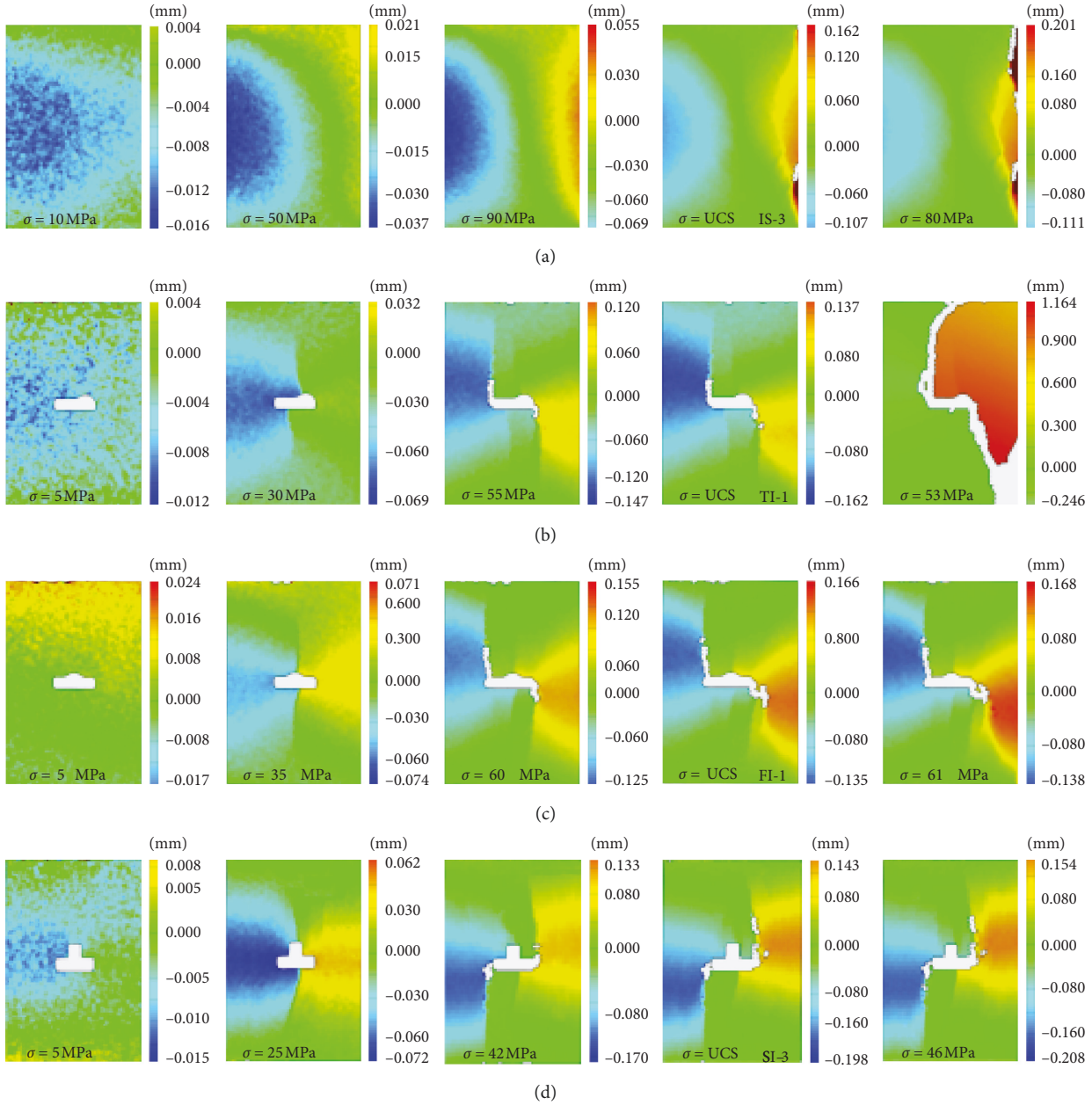

Figure 9: Horizontal displacement contours of four typical specimens at different stress levels: (a) specimen IS-3; (b) specimen TI-1; (c) specimen FI-1; (d) specimen SI-3.

3.5. Evolution Characteristics of Primary Tensile Cracks in Specimens with a Hole. As shown in Figure 8, at the beginning, the primary tensile cracks initiate from tensile stress concentration zones, namely, the roof and floor of the cavity. Afterwards, with increasing loads, both of them grow towards the direction of compression. However, they will not keep propagating with the increase of the axial stress. On the contrary, they disappear gradually after the appearance of secondary tensile cracks. Furthermore, there is an interesting phenomenon that the two primary tensile cracks emerge again at the end of tests. To have a deep understanding of this behavior, it is of tremendous significance to analyze the strain characteristics of tensile cracks during the process of loading. For each typical specimen with a hole, four monitoring points of strain in the horizontal direction were placed on the propagation paths of two tensile cracks, respectively, and the spacing between monitoring points was set as 5 mm. The strain-time curves of eight measurement points (i.e., R1, R2, R3, R4, F1, F2, F3, and F4) in combination with stress for each typical specimen under compression are illustrated in Figure 11. The law of strain for each specimen can be summarized as follows: (1) Before the point (A), the strains of all monitoring points are very small, indicating that the specimens do not deform apparently and only internal pores were compacted under low stress. (2) Starting from point (A), the two tensile cracks begin to propagate and the strain increases rapidly. Thus, the initiation stress of tensile cracks can be picked, which is about

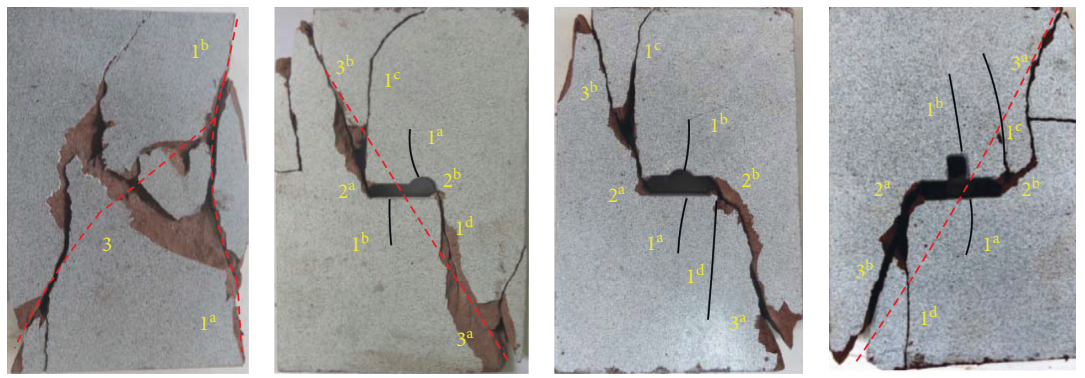

Figure 10: Failure modes of four types of specimens subjected to axial loads: (a) specimen IS-3; (b) specimen TI-1; (c) specimen FI-1; (d) specimen SI-3.

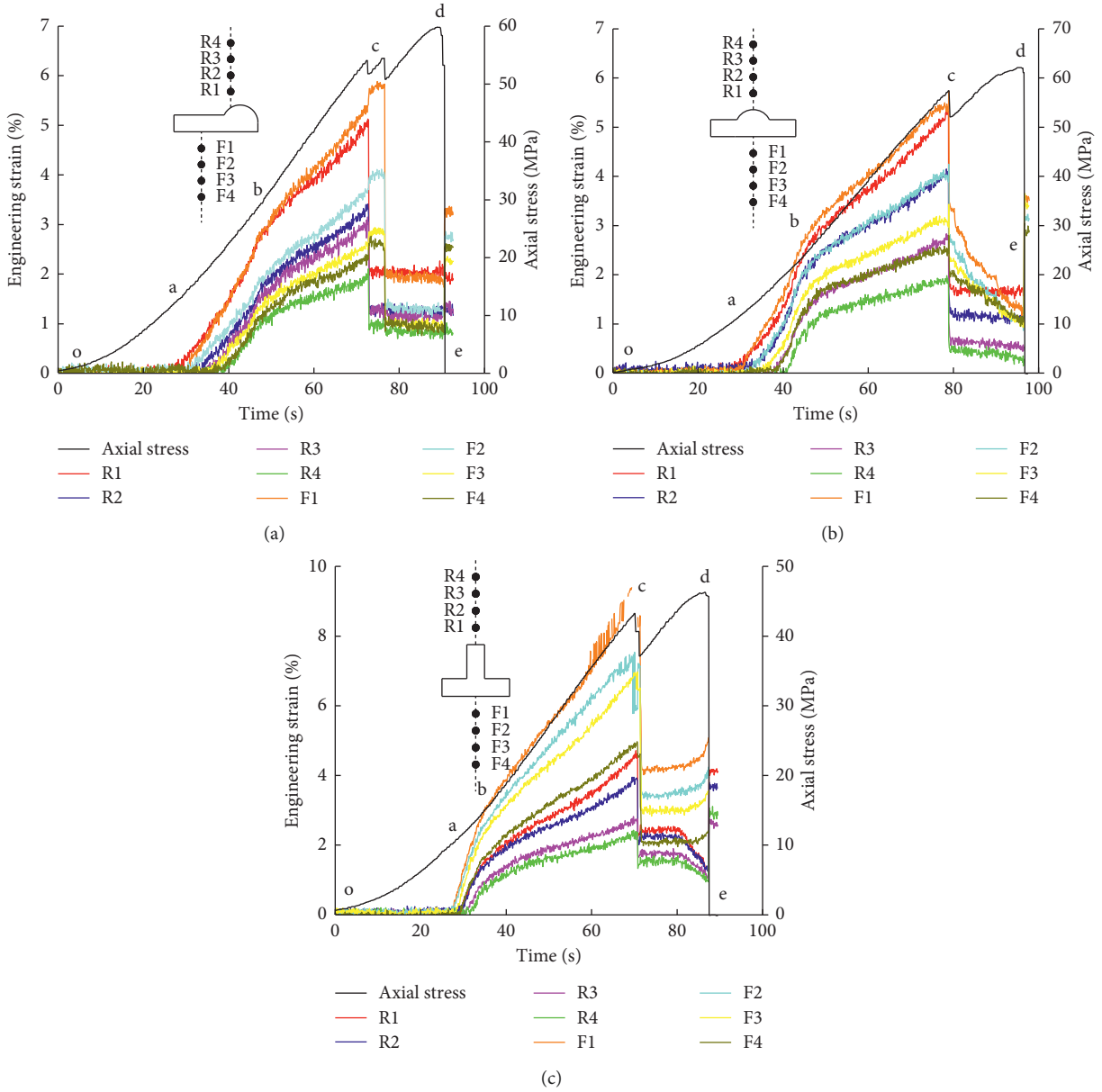

Figure 11: Strain and stress-time curves of monitoring points under uniaxial loading: (a) specimen TI-1; (b) specimen FI-1; (c) specimen SI-3.

0.25UCS. It can be seen that the strain of the point closest to the hole is first increased. Clearly, the propagation of tensile cracks is gradual under progressive loads. (3) There is a turning point (B) in the strain-time curves corresponding to a stress of about 0.5UCS, and the strain growth slows down after the point. Consequently, the cracks might stop propagating forward when they reach a certain length regardless of the increasing loads. (4) Owing to the sudden appearance of secondary cracks at point (C), the strains of all points drop drastically from the peak. Subsequently, the strains slowly decline between points (C) and (D), which are restrained by the slow propagation of secondary cracks. (5) At the post-peak stage, the strains of all points start to increase again, suggesting that the tensile cracks reopen at the end of experiments.

To conclude, the evolution characteristic of tensile cracks can be effectively reflected by the variation of strain. The two tensile cracks emerged in the top and bottom vicinity of holes experience a process of "open-close-reopen" under axial compression. The reasons are listed hereafter. Firstly, tensile cracks will initiate from the places where tensile stress concentrates, such as the roof and floor of the cavity, and then develops towards the maximum compression direction. When the length of cracks is equal to the size of the cavity, the critical stress condition shifts to either side of the tensile crack [37], resulting in the nucleation and propagation of secondary tensile cracks, and the rock on both sides of the cracks will deform outward. Accordingly, the tensile cracks will be closed under squeezing. Only after the shear cracks coalesce with the secondary tensile cracks, restraint of tensile cracks can be removed. That is why the tensile cracks open again when the specimen is of failure.

4. Conclusion

In the study, a series of experiments was carried out to investigate the mechanical properties and fracture responses of sandstone containing an intersecting hole with different shapes under uniaxial compression. DIC technique was used to monitor the real-time evolution of cracks during tests. The conclusions drawn are as follows:

(1) The prefabricated cavity has a significant weakening effect on the mechanical properties of specimens, and the influence is closely related to the hole shapes. The less rounded the boundary of the hole, the lower the strength of the specimen. Group SI has the minimum strength and Young's modulus among the four groups.

(2) For specimens with a hole, the failure can be considered as a progressive process of the initiation and propagation of primary tensile cracks, spalling fracture on both sidewalls of holes, sudden appearance and slow growth of secondary tensile cracks, as well as the nucleation of shear cracks and their coalescence with the secondary tensile cracks into macrofractures. Different from the tensile-shear failure mode of the intact specimens, the failure of specimens containing a hole is dominated by shearing.

(3) The formation of primary tensile cracks is not the key to the ultimate failure of specimens with a cavity. The primary tensile cracks experience a process of "open-close-reopen", which is consistent with the variation of horizontal strains on the propagation path of tensile cracks. The reason is that the appearances of new cracks restrain the development of primary cracks, and the inhibition will be removed when macrofailure occurs.

(4) DIC technique provides a new way to quantitatively analyze the fracture behavior of specimens under loads, and the evolution process can be visually displayed. However, speckles missing caused by local deformation makes it difficult to record complete DIC images at the end of experiments. Moreover, how to accurately determine the critical strain of cracks initiation needs further study in the next work.

Data Availability

The data used to support the findings of this study are available from the corresponding author upon request.

Conflicts of Interest

The authors declared no potential conflicts of interest with respect to the research, authorship, and/or publication of this article.

Acknowledgments

This work was supported by the National Natural Science Foundation of China (no. 51774321), the National Key Research and Development Program of China (no. 2018YFC0604606), and the Fundamental Research Funds for the Central Universities of Central South University (no. 2018zzts215).

References

[1] B. H. G. Brady and E. T. Brown, *Rock Mechanics for Underground Mining*, Kluwer Academic Publishers, Dordrecht, Netherlands, 3rd edition, 2006.

[2] G. Walton, E. Kim, S. Sinha, G. Sturgis, and D. Berberick, "Investigation of shaft stability and anisotropic deformation in a deep shaft in Idaho, United States," *International Journal of Rock Mechanics and Mining Sciences*, vol. 105, pp. 160–171, 2018.

[3] A. Shaterpour-Mamaghani and N. Bilgin, "Some contributions on the estimation of performance and operational parameters of raise borers—a case study in Kure Copper Mine, Turkey," *Tunnelling and Underground Space Technology*, vol. 54, pp. 37–48, 2016.

[4] Z. Niedbalski and T. Majcherczyk, "Indicative assessment of design efficiency of mining roadways," *Journal of Sustainable Mining*, vol. 17, no. 3, pp. 131–138, 2018.

[5] H. Gerçek, "Stability considerations for underground excavation intersections," *Mining Science and Technology*, vol. 4, no. 1, pp. 49–57, 1986.

[6] J. K. Borsah, P. D. Shelton, and N. Tomlin, "Deformation of a deep shaft inset in coal measures rocks during and after construction," *Developments in Geotechnical Engineering*, vol. 32, pp. 167–173, 1981.

[7] A. M. Remennikov, V. Mutton, S. Nimbalkar, and T. Ren, "Experimental and numerical investigation of high-yield grout ore pass plugs to resist impact loads," *International Journal of Rock Mechanics and Mining Sciences*, vol. 70, pp. 1–15, 2014.

[8] K. Hana, D. Conover, and K. Haramy, "Coal mine entry intersection behavior study," Report, United States Bureau of Mines, Pittsburgh, PA, USA, 1991.

[9] S. Okubo and S. S. Peng, "Roof bolting patterns at three-way entry intersections," Report, West Virginia University, Charlottesville, VA, USA, 1978.

[10] H. Gerçek, *Stability of intersections in room-and-pillar coal mining*, Ph.D. thesis, The Pennsylvania State University, State College, PA, USA, 1982.

[11] J. Hematian, *Stability of roadways and intersections*, Ph.D. thesis, University of Wollongong, Wollongong, Australia, 1994.

[12] R. N. Singh, I. Porter, and J. Hematian, "Finite element analysis of three-way roadway junctions in longwall mining," *International Journal of Coal Geology*, vol. 45, no. 2-3, pp. 115–125, 2001.

[13] G. S. Esterhuizen, I. B. Tulu, and T. Klemetti, "Analysis of factors influencing coal mine intersection stability," in *Proceedings of the 48th US Rock Mechanics/Geomechanics Symposium*, Minneapolis, MN, USA, June 2014.

[14] B. Abbasi, "A numerical analysis of mine intersections and support systems for stability," Master thesis, Southern Illinois University, Carbondale, IL, USA, 2010.

[15] T. k. Lu, B. h. Guo, and L. c. Cheng, "Numerical modeling for further understanding of roadway junction stability behaviour at deep underground," *Journal of Coal Science and Engineering (China)*, vol. 14, no. 1, pp. 38–43, 2008.

[16] Z. B. Guo, J. J. Shi, J. Wang, F. Cai, and F. Q. Wang, "Double-directional control bolt support technology and engineering application at large span Y-type intersections in deep coal mines," *Mining Science and Technology (China)*, vol. 20, no. 2, pp. 254–259, 2010.

[17] A. R. Mueller, "An analysis of current intersection support and falls in United States coal mines and recommendations to improve safety," Master thesis, Southern Illinois University Carbondale, Carbondale, IL, USA, 2009.

[18] S. Sinha, "Analyses for design and support of coal mine intersections," Master thesis, Southern Illinois University Carbondale, Carbondale, IL, USA, 2016.

[19] H. B. Chai, Y. B. Zhang, L. C. Cheng, and Y. F. Zou, "Research on deformation and stability of wall rocks in intersection of laneway in deep mine," *Journal of Mining & Safety Engineering*, vol. 27, no. 2, pp. 200–204, 2010.

[20] N. B. Huang and D. H. Kong, "Study of reinforcement control technology and roof deformation of oblique cross with large section," *Journal of Mining & Safety Engineering*, vol. 23, no. 2, pp. 249–252, 2006.

[21] C. Wang, N. Zhang, G. C. Li, and J. Y. Chen, "Numerical simulation and support of roadway intersection," *Journal of Mining & Safety Engineering*, vol. 25, no. 4, pp. 384–388, 2008.

[22] X. Y. Wang, M. C. He, and S. B. Yang, "Failure mode of deep large section intersecting laneway and its countermeasures," *Journal of Mining & Safety Engineering*, vol. 24, no. 3, pp. 283–287, 2007.

[23] M. C. He, G. F. Li, A. W. Ren, and J. Yang, "Analysis of the stability of intersecting chambers in deep soft-rock roadway construction," *Journal of China University of Mining & Technology*, vol. 37, no. 2, pp. 167–70, 2008.

[24] Z. B. Guo, P. Y. Guo, M. H. Huang, and Y. G. Liu, "Stability control of gate groups in deep wells," *Mining Science and Technology (China)*, vol. 19, no. 2, pp. 155–160, 2009.

[25] X. Li, "Deep shaft connecting chambers dynamic response model experiment research," Master thesis, Anhui University of Science and Technology, Huainan, China, 2009.

[26] H. Cheng, H. B. Cai, C. X. Rong, Z. S. Yao, and M. J. Li, "Rock stability analysis and support countermeasure of chamber group connected with deep shaft," *Journal of China Coal Society*, vol. 36, no. 2, pp. 261–266, 2011.

[27] P. G. Ranjith, J. Zhao, M. H. Ju, R. V. S. De Silva, T. D. Rathnaweera, and A. K. M. S. Bandara, "Opportunities and challenges in deep mining: a brief review," *Engineering*, vol. 3, no. 4, pp. 546–551, 2017.

[28] T. B. Yin, L. Bai, X. Li, X. B. Li, and S. S. Zhang, "Effect of thermal treatment on the mode I fracture toughness of granite under dynamic and static coupling load," *Engineering Fracture Mechanics*, vol. 199, no. 8, pp. 143–158, 2018.

[29] X. B. Li, F. Q. Gong, M. Tao et al., "Failure mechanism and coupled static-dynamic loading theory in deep hard rock mining: a review," *Journal of Rock Mechanics and Geotechnical Engineering*, vol. 9, no. 4, pp. 767–782, 2017.

[30] R. Ulusay and J. A. Hudson, *The Complete ISRM Suggested Methods for Rock Characterization, Testing and Monitoring: 1974–2006*, ISRM Turkish National Group, Ankara, Turkey, 2007.

[31] I. Yamaguchi, "A laser-speckle strain gauge," *Journal of Physics E: Scientific Instruments*, vol. 14, no. 11, pp. 1270–1273, 1981.

[32] W. H. Peters and W. F. Ranson, "Digital imaging techniques in experimental stress analysis," *Optical Engineering*, vol. 21, no. 3, pp. 427–431, 1982.

[33] B. Pan, K. Qian, and H. Xie, "Two-dimensional digital image correlation for in-plane displacement and strain measurement: a review," *Measurement Science & Technology*, vol. 20, no. 6, article 062001, pp. 152–154, 2009.

[34] Z. L. Zhou, L. H. Tan, W. Z. Cao, Z. Y. Zhou, and X. Cai, "Fracture evolution and failure behaviour of marble specimens containing rectangular cavities under uniaxial loading," *Engineering Fracture Mechanics*, vol. 184, pp. 183–201, 2017.

[35] J. A. Sanchidrián, P. Segarra, and L. M. López, "Energy components in rock blasting," *International Journal of Rock Mechanics and Mining Sciences*, vol. 44, no. 1, pp. 130–147, 2007.

[36] D. Y. Li, Q. Q. Zhu, Z. L. Zhou, X. B. Li, and P. G. Ranjith, "Fracture analysis of marble specimens with a hole under uniaxial compression by digital image correlation," *Engineering Fracture Mechanics*, vol. 183, pp. 109–124, 2017.

[37] B. J. Carter, E. Z. Lajtai, and A. Petukhov, "Primary and remote fracture around underground cavities," *International Journal for Numerical and Analytical Methods in Geomechanics*, vol. 15, no. 1, pp. 21–40, 1991.